Physics of Fluids ARTICLE pubs.aip.org/aip/pof

Cavitating flow morphology determination in cavitation-on-a-chip devices based on local real-time pressure measurements

Cite as: Phys. Fluids **37**, 022009 (2025); doi: 10.1063/5.0250303
Submitted: 24 November 2024 · Accepted: 6 January 2025 ·
Published Online: 4 February 2025

View Online Export Citation CrossMark

Erçil Toyran,[1,2] Farzad Rokhsar Talabazar,[1,2] Iakovos Tzanakis,[3,4] Morteza Ghorbani,[1,2,3,5] and Ali Koşar[1,2,5,a)]

AFFILIATIONS

[1]Faculty of Engineering and Natural Science, Sabanci University, Tuzla, Istanbul 34956, Turkey
[2]Sabanci University Nanotechnology Research and Application Center, Tuzla, Istanbul 34956, Turkey
[3]Faculty of Technology, Design and Environment, Oxford Brookes University, Headington, Oxford OX3 0BP, United Kingdom
[4]Department of Materials, University of Oxford, Parks Road, Oxford OX1 3PH, United Kingdom
[5]Center of Excellence for Functional Surfaces and Interfaces for Nano-Diagnostics (EFSUN), Sabanci University, Orhanli, Tuzla, Istanbul 34956, Turkey

Note: This paper is part of the Special Topic, Recent Advances in Fluid Dynamics and Its Applications.
[a)]**Author to whom correspondence should be addressed:** kosara@sabanciuniv.edu

ABSTRACT

This study presents a practical approach for the characterization and control of hydrodynamic cavitation (HC) behavior in microfluidic devices by utilizing real-time static pressure measurements. Two geometrically identical micro-orifice devices were specifically designed for this purpose. Pressure measurement locations were strategically positioned along the embedded microchannel in both devices. These locations were determined as a function of the hydraulic diameter of the microchannel. Pressure measurements were simultaneously made with high-speed imaging. Particular attention was directed to the prediction and monitoring of cavitation inception, cavitating flow patterns, and cavitation development. Thus, the dynamic and complex nature of hydrodynamic cavitation in microdomains could be captured by local pressure variations along the microchannel walls. According to the results, cavitation inception and subsequent formation of twin sheet cavities could be detected by changes in local pressure values. Moreover, the analysis of local pressure variations could be employed to predict the length of sheet cavities. The findings of this study offer valuable guidelines for designing microfluidic systems involving hydrodynamic cavitation. Moreover, this study proves the potential of local wall pressure measurements as a stand-alone practical approach, which will reduce reliance on high-speed visualization. It could thus enhance the affordability and accessibility of HC-on-a-chip platforms for emerging applications, including biomedical engineering, wastewater treatment, and 2D material exfoliation.

I. INTRODUCTION

Cavitation is one of the phase change phenomena and involves a successive cycle of formation, growth, and collapse of gas/vapor bubbles. Cavitation bubbles are generated when a fluid experiences a sudden local pressure drop below its vapor saturation pressure and collapse upon pressure recovery.[1] The major types based on generation of the cavitation phenomenon are optic cavitation, acoustic cavitation, and hydrodynamic cavitation (HC).[2] In optic cavitation, a short pulse of laser light is exposed to a liquid medium leading to intense vaporization of the liquid and eventually to the formation of cavitation bubbles.[3] Acoustic cavitation involves the generation of bubbles by irradiating the liquid with an ultrasound field of sufficient intensity.[4] However, HC occurs when the flow velocity increases through a flow constriction, and the resultant local static pressure drop triggers the formation of cavitation bubbles.[5] Cavitation bubbles grow in cycles and result in the formation of local impact pressures and shock waves as mechanical effects of collapse,[1] which produce noise and vibrations.[2] Moreover, highly reactive free radicals such as hydroxyls appear as chemical effects of collapse.[6] Hydrodynamic cavitation has been extensively studied through both experimental and computational fluid dynamic (CFD) approaches, with recent advancements focusing on multiphase flow dynamics and bubble behavior.[7–9] Although HC is

not desired in turbomachinery including propellers and pumps, owing to erosion and malfunctioning,[10,11] it could have enormous potential for use in emerging applications ranging from the food and beverage industry to wastewater treatment.[12,13]

The recent advances in HC studies have provided a better understanding of this phenomenon and attracted the attention of the scientific community due to its energy efficiency,[14] scale-up possibility,[15] and simplicity.[5] The last two decades have witnessed tremendous advances in microfluidic technologies and have opened a new frontier in HC studies, which triggered the emergence of the HC-on-a-chip concept.[16] In this concept, cavitation bubbles are generated in confined microchannels, which offer unique advantages, including a high surface-to-volume ratio and better control and manipulation of cavitation parameters.[16,17] Such small-scale systems have also enabled the use of chemicals such as toxic liquids, which cannot be easily examined in conventional scale HC.[16] In addition, the use of small amounts of liquids has paved the way for the utilization of cavitation in biomedical treatment.[17] This concept also offers promising results in applications such as wastewater treatment,[12] energy harvesting,[18] heat transfer,[19] and 2D nanomaterial exfoliation.[20]

Pioneering studies on microscale HC revealed that microscale HC exhibits different behavior compared to conventional scale HC.[21] In this regard, Mishra and Peles[22] showed that the flow patterns in microscale HC on a chip significantly depend on the size and geometry of micro-restrictive elements. Furthermore, Mishra and Peles[23] demonstrated that the transition from cavitation inception to developed and supercavitation flow patterns occurred rapidly at the microscale. Im *et al.*[24] showed that even small changes in micro-orifice geometry affected cavitation evolution at the microscale. Jin *et al.*[25] reported that the ratio of microchannel length to its diameter had a considerable effect on cavitation. In another study, Dular *et al.*[26] used six geometrically identical venturis of different scales and revealed that the sheet cavity became more stable as the scale decreased. In addition to the geometrical effects, the effect of surface properties on the physics of microscale HC was also investigated.[27] In this regard, the effect of sidewall roughness implementation on cavitation inception and flow patterns and the effect of surface roughness were highlighted.[28] In another study, Aghdam *et al.*[29] modified the surface of a microfluidic device by using silica nanoparticles. They showed that the upstream pressure corresponding to the onset of cavitation could be reduced by modifying the surface of the microfluidic devices. Shafaghi *et al.*[30] captured different cavitation flow patterns with varying intensities at the same upstream pressure using a microfluidic device with eight channels and sidewall roughness.

Thus, HC in microdomains, as shown in previous research efforts,[6,20,27] differs significantly from conventional scale cavitation due to the dominant influence of surface effects and tension at the microscale. In microfluidic systems, bubble behavior is strongly affected by channel dimensions, surface properties, morphology, and boundary interactions. The confined environment not only causes asymmetric bubble collapse (intensifying cavitation) but also produces unique chemical effects due to bubble collapse, as observed in the experimental study of the authors on microscale devices.[6] This contrasts with conventional scale cavitation, where bubbles form and collapse more freely in the bulk liquid environment, and the related dynamics are primarily driven by inertial forces with reduced surface interactions.

The above-mentioned studies were devoted to the physics of cavitation in the microscale. However, they mostly relied on optical techniques such as high-speed imaging, particle image velocimetry (PIV), laser-induced fluorescence (LIF), and shadowgraphy for HC characterization. Although these techniques provide valuable insights into the dynamics and properties of HC, one of the main challenges arises from the multiple scattering and reflection effects in optical characterization.[31] This issue persists in the PIV and LIF visualization techniques, especially upon the addition of scattering light contamination from tracer particles in these techniques.[31] Hence, most PIV and LIF visualization techniques are not very adequate for monitoring the events inside cavitating flows and measuring bubble properties such as velocity field, size, and shape.[31–34] Moreover, these techniques require specialized optical instrumentation, and particularly for HC-on-a-chip devices, they could have limitations in terms of accessibility and affordability. Optical measurement techniques also need at least one transparent side of a microscale cavitation device. Therefore, the design and fabrication of HC-on-a-chip devices that are both transparent and capable of withstanding high pressures constitute another challenge.[35] Auxiliary measurement techniques and tools are required to fully assess the effects of related parameters and shed light on the physics of microscale cavitating flows.

In most of the studies, static pressure measurements were performed upstream and downstream of the microchannels to calculate cavitation number.[23] The cavitation number is a dimensionless number mainly used to characterize the state of HC,[36]

$$\sigma = \frac{P_a - P_v}{\frac{1}{2}\rho V^2}, \tag{1}$$

where P_a and P_v are the ambient and vapor saturation pressures of the liquid, respectively. ρ and V are the density and velocity of the working fluid. Cavitation intensity and effective length increase upon a decrease in cavitation number.[23] According to Sawant *et al.*,[37] the cavitation number could be used as a preliminary index to assess the relative performance of cavitation since it represents the relative intensity of cavitation. Pipp *et al.*[38] used computational and experimental methods to measure the attached sheet cavity length inside a venturi and presented its relationship with the cavitation number. While the cavitation number is a useful tool for quantifying cavitation, there are several drawbacks associated with its functionality since it does not include crucial parameters for HC characterization, such as geometric parameters, temperature, and the presence of impurities in the fluid.[36,39,40] For example, Ge *et al.*[41] showed that temperature variation also affects the HC cavitating flows in a venturi device, including cavity length and thickness, flow regime transition, and cavitation intensity. Moreover, HC is a dynamic process where bubbles develop and collapse rapidly upon the changes in pressure and flow conditions.[36] Therefore, this could result in the misrepresentation of cavitation behavior in systems with highly variable cavitating flow conditions, especially in microscale HC studies. Apart from cavitation number calculation, static local pressure measurements are also used to characterize the cavitating flow inside a commercial-scale nozzle. Bauer *et al.*[42] measured local static pressure variations at six different points on the cavitating nozzle wall using pressure ports placed along the same line within the nozzle. They simultaneously explained the pressure variations during different cavitation stages with visualization and demonstrated that these

cavitation stages can be described by the corresponding pressure curves in a commercial-scale nozzle. In another study, Cioncolini *et al.*[43] investigated the pressure drop across the micro-orifice plates and investigated the discharge characteristics by measuring static pressures at the upstream and four different locations downstream of micro-orifice plates.

While theoretical studies focused on static pressure fluctuations inside the channels to characterize the cavitation processes in microdomains,[25,44] there are no studies that explain cavitating flow patterns by generating static pressure curves inside the microchannels. Accordingly, the development of new characterization methods and procedures is crucial for the facile characterization of HC behavior in the small scale, where most of the characterization depends on flow visualization techniques. To the authors' best knowledge, this study is the first study to capture real-time static pressure measurements along the microchannel walls as a monitoring tool to detect cavitation inception, twin sheet cavitation formation, and cavitation development in HC-on-a-chip. While many studies rely on high-speed imaging and high-frequency pressure pulsation measurements to investigate the cavitating flow morphology, the proposed approach offers a cost-effective and practical real-time monitoring tool for cavitation detection in HC-on-a-chip devices, minimizing or even eliminating the need for complex high-speed visualization. For this, variations in static pressure along a short microchannel at different locations and walls inside cavitation-on-a-chip devices were monitored in real time. Static pressure measurements performed on both microchannel walls facilitated the investigation of cavitation, which can develop differently on each wall. Two microfluidic devices were designed and utilized for this purpose. These devices have the same geometry; however, the in-pressure ports have different configurations. Pressure measurements were performed under cavitating flow conditions at three different point locations along the microchannel for each device. The locations of the pressure ports depend on the hydraulic diameter of the microchannel in the devices. According to the results, the inception and development of cavitation affect the pressure values at these ports. Using these pressure changes with time, the inception and development of cavitation in devices could be monitored. Visualization was also performed simultaneously with a high-speed camera during the measurements. The results showed that local pressure measurements inside the microchannel could be used to detect, investigate, and control the dynamic and complex nature of HC on a chip without the need for visualization, and corresponding flow morphology could be constructed with this approach.

II. MATERIALS AND METHODS

A. Device configuration

The microfluidic devices, as shown in Fig. 1, were designed as twin microfluidic cavitation-on-a-chip platforms. Their channel design parameters are identical, while the locations of the pressure measurement ports are different. The design parameters are included in Fig. 1(c). They consist of three regions: the inlet, microchannel, and extension. The lengths of the inlet and extension parts are 3000 μm, and the length of the microchannel part is 2000 μm. The channel widths are 900 μm for the inlet and extension regions and 400 μm for the microchannel region. The flow-restrictive part (microchannel) is responsible for the sudden pressure drop that triggers cavitation.

In order to measure local pressures in the devices, three pressure ports, one above and two below the microfluidic channel, were formed. The locations of the ports where static pressure measurements were performed and their distances to the walls are displayed in Fig. 1 for the two tested microfluidic cavitation-on-a-chip devices. For the first microfluidic device, the P1, P2, and P3 ports are 6 D_h, 9 D_h, and 15 D_h away from the entrance of the microchannel, respectively, while they are 4 D_h, 13 D_h, and 18 D_h away from the entrance of the microchannel for the second microfluidic chip, respectively. These specific positions were chosen to capture the pressure variations in regions before (upstream), within, and beyond (downstream) the microchannel, the flow-restrictive element responsible for the sudden pressure drop that triggers cavitation. By selecting these distances, the experimental setup ensures the coverage of key transitional zones in the flow, including the initial stabilization zone, primary cavitation development region, and recovery region where there is a pressure rise after the cavitation zone. The use of proportional distances to D_h allows for the comparison of the experimental data with established nondimensional parameters such as Reynolds and Weber numbers, which will be critical for scaling and interpreting cavitation behavior in near-future studies. This setup provides a detailed understanding of pressure dynamics and cavitating flow morphology, covering the full spectrum of the cavitation phenomenon. The hydraulic diameter of the channel was calculated using the following formula: $D_h = \frac{2xWxH}{W+H}$, where W is the width and H is the depth of the microchannel.

B. Microfluidic device design and fabrication procedure

The fabrication process flow of microfluidic devices includes crucial steps such as wafer grinding, SiO_2 coating, photolithography, SiO_2 and silicon etching, protective layer deposition, wet etching, piranha cleaning, and anodic bonding. The process flow is shown in Fig. 1(d). These steps ensure the fabrication of robust microfluidic cavitation-on-a-chip devices capable of withstanding high pressures. Double-side polished silicon wafers with a thickness of 380 μm were used, and a glass wafer with a thickness of 380 μm was anodically bonded on top of the silicon wafer to cover the channels and allow for visualization. The detailed fabrication process of microfluidic devices was reported in our previous work.[35]

C. Experimental setup and procedure

The experimental setup shown in Fig. 2 includes a high-pressure nitrogen tank (Linde Gas, Gebze, Kocaeli, Turkey) to supply the desired inlet pressure to push the liquid through the system. High-pressurized nitrogen gas was introduced to the system in a controlled manner using a pressure regulator and a pressure sensor (Omega, Manchester, UK). The nitrogen tank was connected to a stainless-steel liquid container (Swagelok, Erbusco, Italy) through stainless-steel tubing (Swagelok, Erbusco BS, Italy). To ensure a secure and controlled setup, the microfluidic device was sealed within an aluminum package, equipped with appropriate inlet and outlet ports (Fig. 2). Micro O-rings and suitable connectors (Swagelok, Erbusco, Italy) were utilized to prevent any leakage in the system. Fine valves and stainless-steel tubing were used to establish connections between the package and the fluid container. A pressure sensor (Omega, Manchester, UK) (with an accuracy value of $\pm 0.25\%$ and a range of up to 3000 kPa) was

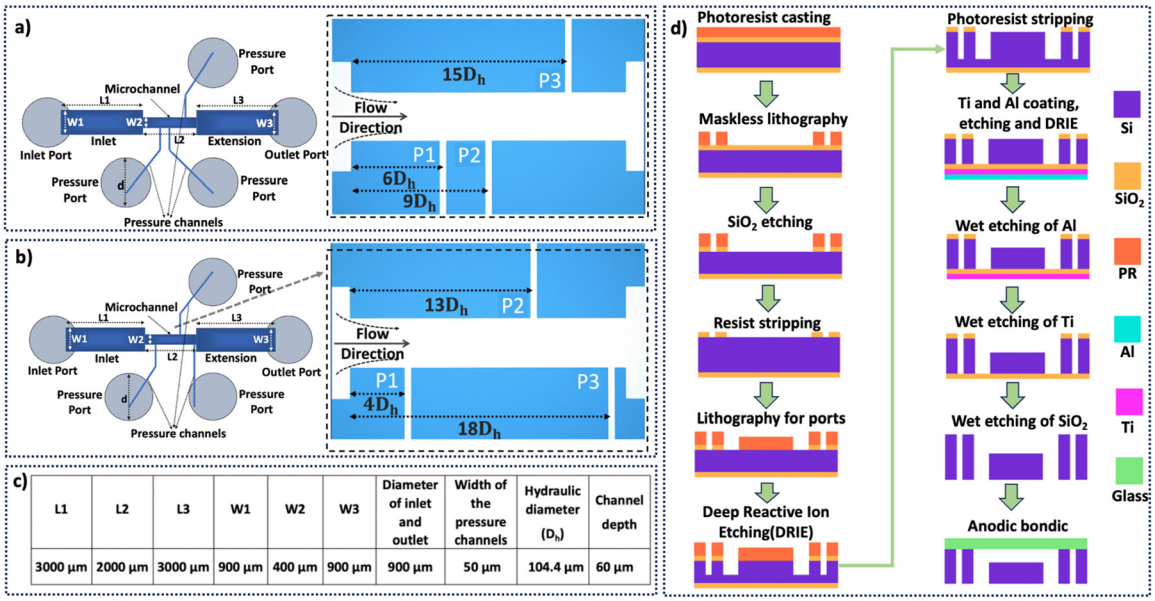

L1	L2	L3	W1	W2	W3	Diameter of inlet and outlet	Width of the pressure channels	Hydraulic diameter (D_h)	Channel depth
3000 μm	2000 μm	3000 μm	900 μm	400 μm	900 μm	900 μm	50 μm	104.4 μm	60 μm

FIG. 1. Geometrical parameters and pressure measurement locations of the microfluidic cavitation-on-a-chip devices: (a) the first microfluidic device and (b) the second microfluidic device. The microfluidic device consists of an inlet, microchannel, and extension region. Inlet and outlet ports are shown on the left and right sides, respectively. Other ports serve for real-time pressure measurement purposes. (c) Geometrical parameters of the microfluidic device. (d) Fabrication process flow of cavitation-on-a-chip devices.

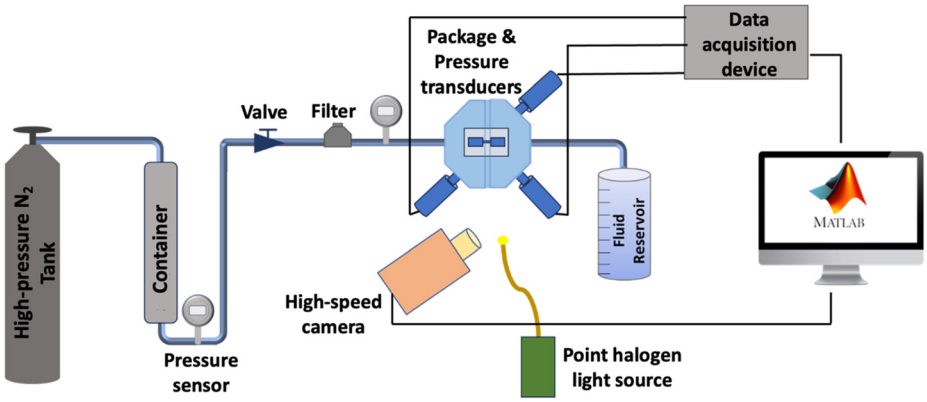

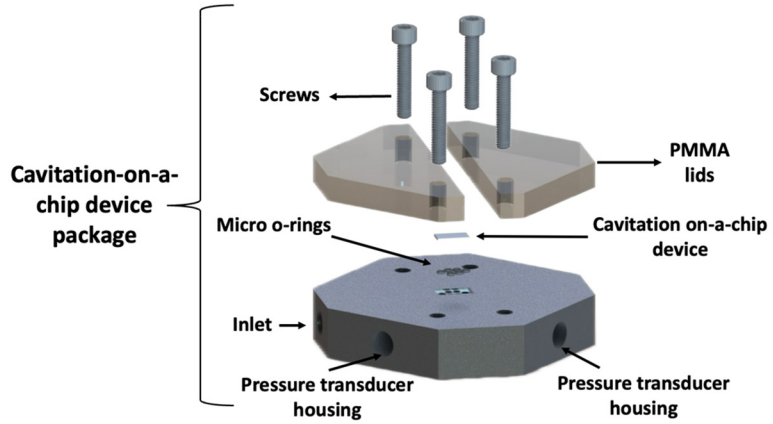

FIG. 2. The exploded view of the package of cavitation-on-a-chip device and the experimental setup consisting of a hydrodynamic cavitation (HC) test section and real-time pressure measurement system including pressure transducers and a high-speed camera.

incorporated into the experimental setup to measure the upstream pressure. Moreover, three PX309 type absolute pressure transducers with a range of up to 690 kPa (Omega, Manchester, UK, 0.25% accuracy and 1 msec response time) were installed in the suitable housings within the package (Fig. 2). The utilized pressure transducers have a sensitivity of 14.5 mV/kPa, which means that for every 1 kPa, a change in the pressure leads to a 14.5 mV change in the output signal. This sensitivity ensured that small changes associated with the cavitation inception and its development could be conveniently captured. These housings were connected to the pressure ports in the HC-on-a-chip devices via pressure channels, as shown in Fig. 1. These pressure transducers allowed the local measurements of pressure changes during cavitation at the pressure port locations. It should be noted that the current pressure sensor configuration is not capable of effectively capturing or resolving shock waves. However, the previous research of the authors has demonstrated that it is feasible to use fiber optic sensors,[45–47] which the authors will plan to explore in a near-future study. Keysight 34970 A Data Acquisition/Data Logger Switch Unit was employed to acquire data from these pressure transducers. Keysight 34901 A plug-in module, which is a multiplexer for general-purpose scanning, was inserted into a mainframe slot of the data acquisition device. This data acquisition unit was connected to a workstation through RS232 interfaces so that the data were collected and monitored using the MATLAB software.

Flow visualization inside the microfluidic cavitation-on-a-chip devices could be made thanks to the glass wafer that allowed flow monitoring within the channel. To record cavitating flow patterns during the experiments, a double-shutter CMOS high-speed camera (Phantom VEO-710L) was employed. The camera had a resolution of 1280 × 800 pixels, with a pixel size of 0.02 mm. A macro-camera lens (type K2 DistaMax) with a focal length of 50 mm and an f-number of 1.2 was used in conjunction with the camera for optimal recording. The camera was positioned at a distance of 200 mm from the aluminum package to capture the focal area, and only the central region of the lens was utilized for visualization. The images were acquired at a rapid frame rate of 2000 fps, with a shutter speed of 2000 s^{-1} and an exposure time of 500 μs. To ensure suitable illumination, a point halogen light source was positioned in front of the fluidic devices, providing the necessary front light for better visualization with the high-speed camera.

The working fluid (in this study, water) was filled into a liquid container with the use of a high-pressure nitrogen tank that was connected to the top of the container, which pushed the liquid into the system. The upstream pressure was controlled by a high-pressure nitrogen tank connected to a stainless-steel liquid container. The pressure applied at the inlet was regulated to ensure a steady flow of the working fluid into the microfluidic device. In-channel pressure measurements for both devices were initiated at an upstream pressure of 850 kPa, with no cavitation present. The upstream pressure was then gradually increased, and the experiments were concluded at 1760 kPa. Regarding the outlet, it was connected to the atmosphere, providing an atmospheric outlet pressure. This setup can generate a pressure drop across the microchannel, which is the primary driving force for cavitation within the flow-restrictive section of the device. The test temperature was maintained at room temperature, approximately 22 °C ± 1 °C, as the experiments were conducted in a controlled laboratory environment. These conditions ensured the consistency in flow behavior and cavitation dynamics during the experiments. The working fluid passed through valves, a pressure sensor for static pressure upstream pressure measurements, and a filter (with a 14 μm pore size) before entering the chip holder package. In the package, the working fluid entered the microfluidic device, where HC occurred thanks to the use of an embedded microchannel as the flow-restrictive element, and then exited through the device outlets. During the cavitation process, the cavitating flows were visualized by a high-speed camera. The collected data were directly transferred to the workstation for image analysis. The pressure variations were recorded via the integrated pressure transducers. During all experiments, visualization and corresponding pressure variations were recorded simultaneously. All the pressure transducers were calibrated before the experiments.

III. RESULTS AND DISCUSSION

Figure 3 displays the pressure variations at the three different locations [Figs. 1(a) and 1(b)] within device 1. The corresponding HC flow images for each time section are provided in Fig. 4. Accordingly, HC inception, formation of twin sheet cavities, and developed cavitation can be detected.

First, the system started to run, and the time t_0 was the moment when cavitation first occurred in the system. At this time, cavitation inception can be observed as a small sheet cavity at the upper wall of the microchannel [Fig. 4(a)]. At this moment, the measured pressures are 227.5, 185.2, and 92.13 kPa, for the ports P1, P2, and P3, respectively. According to Fig. 3, there is a small pressure drop just before the t_0, at the ($t = t_0$ - 0.5 s, P1 = 224.7 kPa), and then a recovery when the sheet cavity becomes stable. This observed anomaly in the pressure of P1 highlights the cavitation inception near this port [Fig. 4(a)].

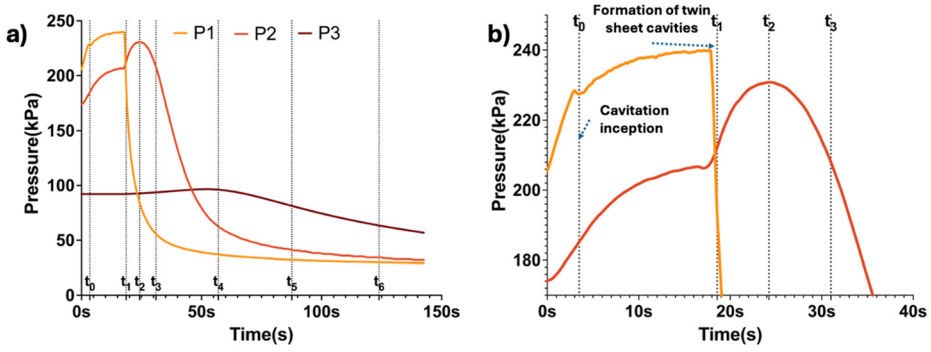

FIG. 3. (a) Changes in pressure at pressure ports 1, 2, and 3 during hydrodynamic cavitation (HC) in device 1 from the start of the test. (b) Magnification between 0 and 40 s. The vertical dashed lines represent the selected time sections.

After the pressure recovery at around t_0, the pressure starts to increase again until 240 kPa, which is the maximum pressure value measured at the P1 port. At this time, the inception cavitating flow pattern exists along the microchannel as a single-sheet cavity. Just beyond this point, the pressure suddenly drops from 240 kPa to 194 kPa within 0.69 seconds (Fig. 3). When the pressure at the P1 port becomes 193.5 kPa at t_1, the pressure values in the other ports, P2 and P3, are 212.2 and 92.18 kPa, respectively. Figure 4(b) shows the HC phenomenon at the mentioned pressures, where twin sheet cavities form at both walls of the microchannel. The formed sheet cavity at the lower wall develops and passes the P1 location, while the measured pressure value for P1 continues to drop. However, the pressure ascends at P2 (Fig. 3). The increase in P2 continues until reaching a maximum value of 231 kPa at t_2 when the pressures at P1 and P3 become 84.3 and 92.8 kPa, respectively. At this moment, the sheet cavity develops and gets closer to the P2 location [Fig. 4(c)]. When the cavitating flow touches the P2 port, the measured pressure at this location suddenly drops. This drop happens between t_2 and t_3, where the sheet cavity is in shedding mode between the P1 and P2 locations. A sudden pressure reduction happens at these ports upon the arrival of the cavity on the lower wall of the microfluidic device. At port 3, which is the nearest pressure measurement location to the outlet of the microchannel, the pressure increases slightly upon an increase in the upstream pressure. However, at time t_4, it starts to decrease similar to the other pressure port (Fig. 3) when the P3 pressure reaches 96.3 kPa. At this moment, the sheet cavity arrives at the P3 location [Fig. 4(e)]. After t_4, it extends slowly, followed by a slight pressure drop in P3. At the time of t_5, the pressure at the P1 port further drops and reaches an almost steady state around 32 kPa whereas the pressures at the other ports continue dropping. At this time, it can be observed that the sheet cavity on the upper wall is above the P3 port location [Fig. 4(f)].

Although cavities on both walls of the microfluidic device move along the microchannel length at t_5, the local pressure at P3 has still a decreasing trend. In addition, the decreasing trend in P3 even after t_6 suggests that the cavity length is extended beyond the location of P3 [Fig. 4(g)], where the pressure values for both P1 and P2 are stabilized after t_6, reaching the pressure of 29 and 32 kPa, respectively. However, P3 becomes 56.5 kPa at the end of the test after it starts to become stable (Fig. 3). The cavity length is mostly considered as a major parameter to represent the intensity of cavitation.[41] However, the estimation of its exact length is challenging. The approach presented here could be a suitable methodology to characterize the cavity length by utilizing different pressure ports without relying on visualization and cavity length measurements.

The pressure variations with time since the start of the system are depicted in Fig. 5 for the second microfluidic cavitation-on-a-chip device, which has the same geometry as the first microfluidic device but different pressure port locations. This device was designed and fabricated to be able to monitor the pressure at different locations within the microchannel. This design aimed to provide a further understanding of the pressure variations of HC along the microchannel. The pressure ports were placed at positions of 4 D_h, 13 D_h, and 18 D_h from the microchannels entrance, denoted as P1, P2, and P3, respectively [Fig. 1(b)].

Corresponding images are provided in Fig. 6. Similar HC features, cavitation inception, twin sheet cavities, and developed cavitation can be observed for device 2.

After starting the system, cavitation inception is detected at the time t_0 when the pressures at P1, P2, and P3 ports are 208.6, 112.7, and 76.8 kPa, respectively. At t_0, cavitation inception is observed on the upper wall as in the previous case [Fig. 6(a)]. In this case, the pressure at P1 first increases and reaches its maximum value of 234 kPa

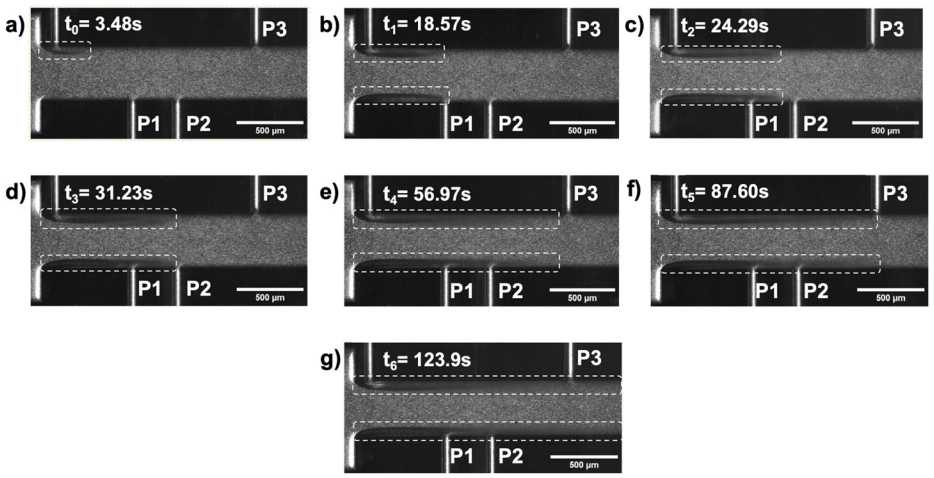

FIG. 4. HC flow visualization at different time sections from the start of the test. (a) When cavitation inception is detected on the upper wall at time t_0 (P1 = 227.5 kPa, P2 = 185.2 kPa, and P3 = 92.3 kPa). (b) Formation of twin sheet cavities when sheet cavities are detected on both microchannel walls when the pressure at P1 reduces to 193.5 kPa and at P2 increases to 212.2 kPa, 15 seconds after cavitation inception. (c) Developed twin sheet cavities beyond the P1 port location when the pressure at P1 further reduces to 84.3 kPa and the pressure at P2 increases to its maximum of 231.2 kPa. (d) Sheet cavities developed at the location of the P2 port, accompanied by a reduction in pressure values at P2, similar to those at the P1 port (P1 = 55.4 kPa, P2 = 207 kPa, and P3 = 93.7 kPa). (e) Developed sheet cavities beyond the location of the P2 port. Sheet cavities extend beyond the P2 port location and move closer to the P3 port location. At this time, the pressure at the P3 port reaches its maximum (P1 = 37kPa, P2 = 67kPa, and P3 = 96.3 kPa). (f) Developed sheet cavities at the location of P3 port, while pressure at P3 port is in a decline trend, and pressures at P1 and P2 ports start to stabilize (P1 = 32kPa, P2 = 41kPa, and P3 = 81.3 kPa). (g) Fully developed sheet cavities beyond all the pressure port locations with stabilization observed in all pressure values. (P1 = 30 kPa, P2 = 33 kPa, and P3 = 63.8 kPa).

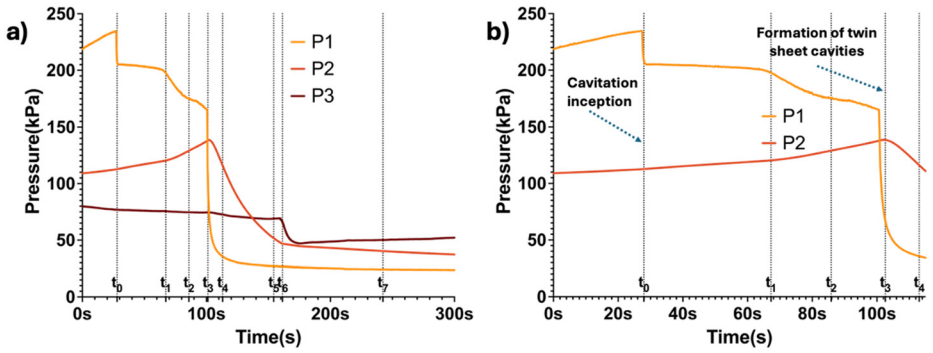

FIG. 5. (a) Pressure changes at pressure ports 1, 2, and 3 in device 2 since the start of the system. The vertical dashed lines represent the selected time sections. (b) Magnification of P1 and P2 data between 0 and 115 s.

(t_0-0.45s) followed by a more pronounced pressure drop. This change is a sign of cavitation inception close to the P1 port on the upper wall [Fig. 6(a)] as in the previous case. However, the pressure at the P1 port does not recover after the appearance of the sheet cavity on the upper wall. It should be mentioned that after cavitation inception occurs, the sheet cavity on the upper wall slowly extends along the channel [Fig. 6(b)]. At this time (t_1), the pressure value at P1 slightly drops to 197.7 kPa. However, the pressure at the P2 port increases to 120.5 kPa. Subsequently, a moderate pressure drop starts at P1 while the pressure at P2 continues to increase. At t_2 in Fig. 5, the pressure at P1 drops to 175.5 kPa, and P2 increases to 129 kPa. Figure 6(c) shows that the sheet cavity develops further along the channel. These observations show that the appearance of cavitation inception and the development of sheet cavity on one of the walls could be detected with the pressure sensors located on the opposite wall of the microchannel. The development of the single-sheet cavity continues until t_3. At this time, as shown in Fig. 6(d), twin sheet cavities form inside the microfluidic channel when the pressure values at the P1, P2, and P3 ports are 95 kPa, 138.3, and 74.3 kPa, respectively. Similar to the previous device, before the formation of twin sheet cavities, a sudden pressure drop is observed at P1 port (Fig. 5). In this case, pressure values at P1 port drop from 167 kPa to 95 kPa when twin sheet cavities form. However, the pressure at P2 port at this time reaches its maximum value of 138.6 kPa (Fig. 5-t_3). Accordingly, at time t_3, as indicated in Fig. 6(d), the sheet cavity on the upper wall becomes closer to P2 port, which is consistent with the previous device. After t_3, the pressure values at P2 port start to drop, and the drop at P1 port continues (Fig. 5). The sheet cavity on the upper wall exceeds beyond the location of P2 and extends

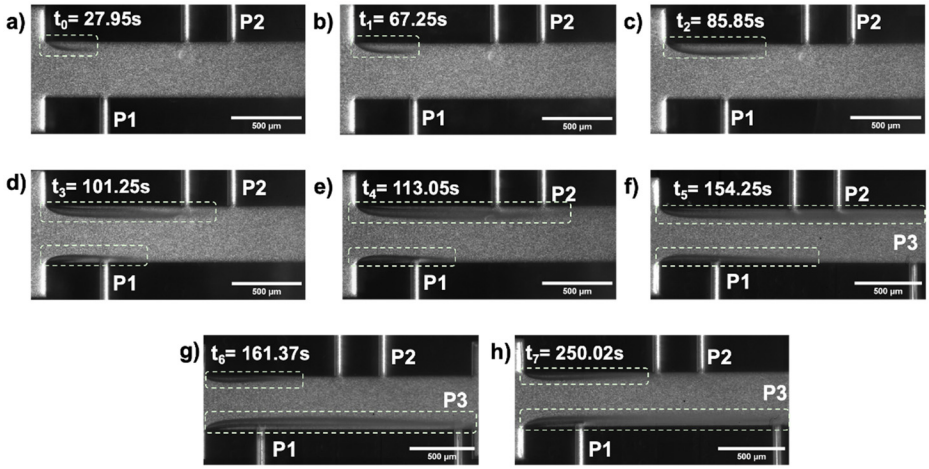

FIG. 6. HC visualization at different times from the start of the test. (a) Cavitation inception on the upper wall when the pressure at the P1 location drops from 234 kPa to 208.6 kPa (P1 = 208.6 kPa, P2 = 112.7 kPa, and P3 = 76.8 kPa). Until t_3, this single-sheet cavity develops along the microchannel, accompanied by a reduction in pressure at location P1 and an increase in pressure at location P2. (b) Developed single-sheet cavity (P1 = 197.7 kPa, P2 = 120.5 kPa, and P3 = 75.5 kPa) near the P1 pressure port location level. (c) Developed sheet cavity on the upper wall beyond the level of P1 port (P1 = 175.5 kPa, P2 = 129 kPa, and P3 = 74.7 kPa). (d) Formation of twin sheet cavities after a sudden pressure drop at the P1 location and sheet cavity on the upper wall develops near the location of the P2 port when the pressure at the P2 location reaches its maximum. (P1 = 95 kPa, P2 = 138.6 kPa, and P3 = 74.3 kPa). (e) Developed sheet cavity beyond the location of P2 port accompanied by pressure decrease at P2 port (P1 = 35.6 kPa, P2 = 116 kPa, and P3 = 72.6 kPa). (f) Fully developed sheet cavity on the upper wall (P1 = 27 kPa, P2 = 52 kPa, and P3 = 69 kPa). (g) Where a sudden flow pattern change occurs: a fully developed sheet cavity on the lower wall accompanied by a sudden pressure drop at P3 location and a shortened sheet cavity on the upper wall (P1 = 26.8 kPa, P2 = 47 kPa, and P3 = 66 kPa). (h) End of the test. Fully developed sheet cavitation on the lower wall and sheet cavity on the upper wall (P1 = 24 kPa, P2 = 40 kPa, and P3 = 51 kPa).

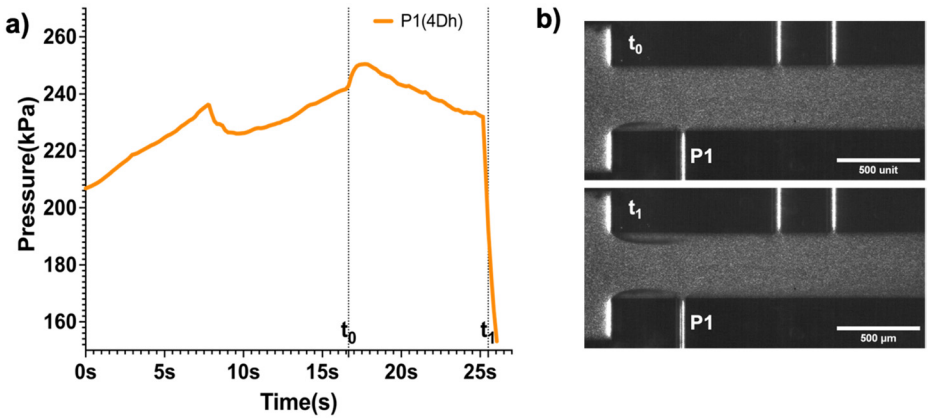

FIG. 7. Pressure variations at pressure port 1 (at the location of 4 D_h) when cavitation first appears on the lower wall in device 2. After a small pressure decrease (5 s), cavitation is first visually detected at t_0. The smooth pressure rise is obtained as the cavitating flow approaches the P1 port, followed by a steady decrease in pressure as the cavitating flow extends. The pressure then sharply decreases, and cavitating flow is observed on the upper wall at time t_1.

further, as shown in Fig. 6(e), at time t_4. After this time, the pressure at P1 port becomes stabilized (27 kPa), and the cavity covers at least one side of the wall [Fig. 6(f)] at time t_5.

At time t_6, the developed sheet cavity on the upper wall shortens, and the sheet cavity on the lower wall extends to the end of the microchannel [Fig. 6(g)]. This behavior reveals the dynamic nature of sheet cavities. Simultaneously, the pressure values at P2 and P3 ports change after t_6 when this event happens. (Fig. 5). Accordingly, pressure values start to increase slightly after a small pressure drop at P3 port. However, the decreasing trend at P2 port continues, albeit at a reduced rate. After t_7, these pressure values start to be stable. P1, P2, and P3 pressure values are 24, 37, and 53 kPa at the end of the test, respectively [Fig. 6(h)].

In contrast to other pressure ports, the local pressure has a decreasing trend with the upstream pressure at port 3 (Fig. 5). It can be observed that although there is a considerable cavity length on both sides and the arrival of the cavity at P3 port at t_7, the local pressure at this port does not get below 50 kPa. This fact is also valid for the previous device.

The major reason for the difficulty in the detection of inception and flow pattern evolution lies in the stochastic nature of cavity formation and unsteady pressure fields in cavitating flows. It is almost impossible to have the same cavity formation, development, and collapse in identical devices under the same conditions, such as the upstream pressure. Therefore, rather than using the upstream or downstream pressures responsible for determining the cavitating flow patterns, the focus should be on the real-time local pressure measurements inside the device. Considering the cavitation inception detection using the approach (in Figs. 3 and 5), it is proven that although in-channel pressure measurement locations are 4 D_h and 6 D_h away from the inlet of the microchannel, they could detect the pressure decrease, which is a sign of incipient cavitation according to conducted experiments. In Figs. 4 and 6, cavitation inceptions are first detected on the upper wall of the microfluidic channel. It can also be observed that before the cavitation inception first occurs on the wall below, a similar pressure decrease can be obtained at the location of 4 D_h from the inlet (Fig. 7). These small pressure decreases could be used to predict cavitation inception since cavitation inception is detected in the devices upon these decreases during all the experiments.

After cavitation inception, the cavitating flow extends through the microchannel (Figs. 4 and 6). Meanwhile, the pressure values recorded at the wall pressure ports for locations of 4 D_h, 6 D_h, 9 D_h, 13 D_h, and 15 D_h from the inlet increase. Afterward, a noticeable decline in pressure values is observed at these locations of the pressure ports when they reach their maximum values. Consequently, the maximum measured pressure at each location occurs when the corresponding cavitating flow reaches these locations. Subsequently, the pressure at these ports begins to decrease, coinciding with sheet cavities contacting the pressure ports. This can be attributed to the growth of low-pressure regions along the channel as the upstream pressure increases.[43] Moreover, it can be caused by the formed bubbles within the microchannel; hence, the existence of these bubbles leads to a pressure decrease. The mentioned trend was attributed to the surface tension effect by Gravesen *et al.*[48] These observations and pressure measurements indicate that the maximum pressure that can be measured is dependent on whether the formed cavitating flow is developed near this location within the channel or not. Since the locations of these pressure ports along the channel are known, maximum pressure values and local pressure variations could be used to predict the cavity length and cavitating flow patterns.

Accordingly, Fig. 8 displays the predicted cavity length and cavitating flow patterns obtained from the local pressure measurements in both devices. In device 1, the formed sheet cavities on both walls develop in almost the same manner over time. Local pressure variations in this device (Fig. 3) do not show any sudden local pressure changes. However, these pressure trends are different in device 2. The sheet cavity on the upper wall develops more compared to the lower wall up to 155 s. After this time, P2 and P3 ports experience sudden pressure changes where a change in flow pattern is predicted in device 2 based on the local pressure values at these port locations. The reduction in the decrease rate of the pressure at the P2 port indicates that the sheet cavity is not at the location of the P2 port, and it is shortened (at 162 s). Moreover, the sudden pressure decrease at the P3 port indicates that the sheet cavity develops to this location on the lower wall at 162 s. It is clear that the schematics are similar to the flow images obtained from high-speed visualizations (Figs. 4 and 6). This proves that cavitating flow physics and characteristics can be captured with local pressure measurements without any visualization by a high-speed camera. This approach can automatically detect any change in cavitating flow behavior and construct flow morphology in real time.

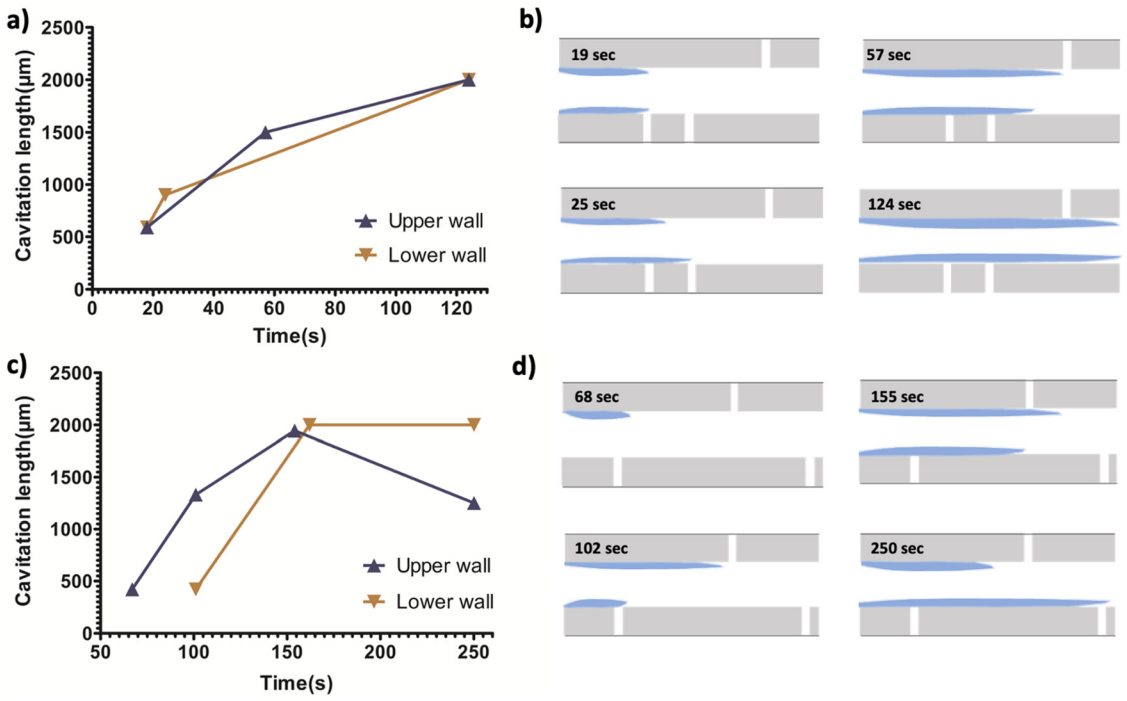

FIG. 8. The cavity length obtained from local pressure measurements for device 1(a) and device 2 (b). Schematics of constructed flow morphology for device 1(b) and device 2 (c) based on the pressure measurements.

IV. CONCLUSION

In this study, cavitation inception, cavitating flow patterns, and developed cavitation were characterized through the monitoring and measurement of local pressure variations on the microchannel walls in microfluidic cavitation-on-a-chip devices. To achieve this, two geometrically identical microfluidic devices with different pressure measurement locations were utilized. The locations of the pressure ports were determined based on the distance from the microchannel entrance in terms of hydraulic diameter D_h. Pressure ports were located at distances of $6\,D_h$, $9\,D_h$, and $15\,D_h$ from the entrance in device 1 and at distances of $4\,D_h$, $13D_h$, and $18\,D_h$ in device 2. In the light of pressure measurements at different ports along the microchannels, it was possible to determine the HC flow morphology, intensity, and dynamic changes (i.e., sudden expansion or shrinkage of sheet cavities) without performing any visualization with a high-speed camera.

The presented method offers a straightforward approach for observing and predicting cavitating flow behavior within microchannels through real-time local pressure measurements. Accordingly, cavitation inception can be detected by wall static pressure variations near the entrance of the microchannel. Local pressures at distances of $4\,D_h$ and $6\,D_h$ from the entrance experience a small decrease, indicating cavitation inception. Afterwards, the observed pronounced decrease at these pressure ports suggests the formation of twin sheet cavities inside the microchannel. The trends (increases, maxima, decreases, and stabilization) in local pressure values reveal key insights about the sheet cavity development and prediction of flow patterns. The findings of this study could provide valuable guidelines for designing microfluidic systems, particularly in applications involving HC. In addition, pressure monitoring along the microfluidic channels could be a stand-alone HC diagnostic method. As a result, this study underlines the potential of local pressure measurement in the detection and control of HC in new-generation microfluidic devices. This approach could substantially reduce the reliance on high-speed visualization, which will render the design and operation of HC-based systems more functional, robust, and cheaper.

ACKNOWLEDGMENTS

This work was supported by the BAGEP Award of the Science Academy, The Royal Society via the Isaac Newton International Fellowship to the project (Grant No. NIF\R1\221238), The British Council (Grant No. 1203770538), and TUBITAK (The Scientific and Technological Research Council of Turkey) in the framework of 1004 ODTUMEMS (Middle East Technical University Microelectromechanical Systems Center) Maestro-Micro Medical Technologies Platform, Project Code 22AG029.

AUTHOR DECLARATIONS

Conflict of Interest

The authors have no conflicts to disclose.

Author Contributions

Erçil Toyran: Data curation (equal); Formal analysis (equal); Investigation (equal); Methodology (equal); Software (equal); Validation (equal); Visualization (equal); Writing – original draft

(equal). **Farzad Rokhsar Talabazar:** Data curation (equal); Formal analysis (equal); Investigation (equal); Methodology (equal); Software (equal); Writing – original draft (equal). **Iakovos Tzanakis:** Conceptualization (equal); Investigation (equal); Methodology (equal); Resources (equal); Writing – original draft (equal). **Morteza Ghorbani:** Conceptualization (equal); Investigation (equal); Methodology (equal); Project administration (equal); Resources (equal); Supervision (equal); Writing – original draft (equal); Writing – review & editing (equal). **Ali Kosar:** Conceptualization (equal); Funding acquisition (equal); Methodology (equal); Project administration (equal); Supervision (equal); Writing – original draft (equal); Writing – review & editing (equal).

DATA AVAILABILITY

The data that support the findings of this study are available from the corresponding author upon reasonable request.

REFERENCES

[1]C. E. Brennen, *Cavitation and Bubble Dynamics* (Cambridge University Press, 2013), pp. 1–249.
[2]F. R. Young, *Cavitation* (Imperial College Press and Distributed by World Scientific Publishing Co., 1999).
[3]C. D. Ohl, V. Venugopalan, and P. A. Quinto-Su, "Generation of laser-induced cavitation bubbles with a digital hologram," Opt. Express. **16**(23), 18964–18969 (2008).
[4]M. Ashokkumar, "The characterization of acoustic cavitation bubbles – An overview," Ultrason. Sonochem. **18**(4), 864–872 (2011).
[5]P. R. Gogate and A. B. Pandit, "A review and assessment of hydrodynamic cavitation as a technology for the future," Ultrason. Sonochem. **12**(1–2), 21–27 (2005).
[6]F. Rokhsar Talabazar, A. Sheibani Aghdam, M. Jafarpour, D. Grishenkov, A. Koşar, and M. Ghorbani, "Chemical effects in 'hydrodynamic cavitation on a chip': The role of cavitating flow patterns," Chem. Eng. J. **445**, 136734 (2022).
[7]Z. Wang, H. Cheng, and B. Ji, "Euler-Lagrange study of cavitating turbulent flow around a hydrofoil," Phys. Fluids **33**(11), 112108 (2021).
[8]Z. Wang, H. Cheng, B. Ji, and X. Peng, "Numerical investigation of inner structure and its formation mechanism of cloud cavitating flow," Int. J. Multiphase Flow **165**, 104484 (2023).
[9]X. Zhao, H. Cheng, B. Ji, L. Li, and R. E. Bensow, "Insights into the characteristics of sheet/cloud cavitation and tip-leakage cavitation based on a compressible Euler-Lagrange model," Phys. Rev. Fluids **9**(10), 104304 (2024).
[10]Z. F. Zhu and S. L. Fang, "Numerical investigation of cavitation performance of ship propellers," J. Hydrodyn. **24**(3), 347–353 (2012).
[11]X. W. Luo, B. Ji, and Y. Tsujimoto, "A review of cavitation in hydraulic machinery," J. Hydrodyn. **28**(3), 335–358 (2016).
[12]M. Dular, T. Griessler-Bulc, I. Gutierrez-Aguirre, E. Heath, T. Kosjek, A. Krivograd Klemenčič, M. Oder, M. Petkovšek, N. Rački, M. Ravnikar, A. Šarc, B. Širok, M. Zupanc, M. Žitnik, and B. Kompare, "Use of hydrodynamic cavitation in (waste)water treatment," Ultrason. Sonochem. **29**, 577–588 (2016).
[13]N. Asaithambi, P. Singha, M. Dwivedi, and S. K. Singh, "Hydrodynamic cavitation and its application in food and beverage industry: A review," J. Food Process Eng. **42**(5), e134 (2019).
[14]S. S. Save, A. B. Pandit, and J. B. Joshi, "Use of hydrodynamic cavitation for large scale microbial cell disruption," Food Bioprod. Process. **75**(1), 41–49 (1997).
[15]H. Zheng, Y. Zheng, and J. Zhu, "Recent developments in hydrodynamic cavitation reactors: Cavitation mechanism, reactor design, and applications," Engineering **19**, 180–198 (2022).
[16]F. Augier, F. Ayela, W. Cherief, D. Colombet, G. Ledoux, M. Martini, S. Mossaz, D. Podbevsek, X. Qiu, and O. Tillement, "Hydrodynamic cavitation through 'labs on a chip': From fundamentals to applications," Oil Gas Sci. Technol. – Rev. IFP Energies Nouvelles **72**(4), 19 (2017).
[17]S. Seyedmirzaei Sarraf, F. Rokhsar Talabazar, I. Namli, M. Maleki, A. Sheibani Aghdam, G. Gharib, D. Grishenkov, M. Ghorbani, and A. Koşar, "Fundamentals, biomedical applications and future potential of micro-scale cavitation-a review," Lab Chip **22**(12), 2237–2258 (2022).
[18]M. T. Gevari, M. Ghorbani, A. J. Svagan, D. Grishenkov, and A. Kosar, "Energy harvesting with micro scale hydrodynamic cavitation-thermoelectric generation coupling," AIP Adv. **9**(10), 105012 (2019).
[19]B. Schneider, A. Koşar, C. J. Kuo, C. Mishra, G. S. Cole, R. P. Scaringe, and Y. Peles, "Cavitation enhanced heat transfer in microchannels," J Heat Transfer **128**(12), 1293–1301 (2006).
[20]M. Jafarpour, A. S. Aghdam, M. T. Gevari, A. Koşar, M. K. Bayazit, and M. Ghorbani, "An ecologically friendly process for graphene exfoliation based on the 'hydrodynamic cavitation on a chip' concept," RSC Adv. **11**(29), 17965 (2021).
[21]C. Mishra and Y. Peles, "An experimental investigation of hydrodynamic cavitation in micro-Venturis," Phys. Fluids **18**(10), 103603 (2006).
[22]C. Mishra and Y. Peles, "Size scale effects on cavitating flows through microorifices entrenched in rectangular microchannels," J. Microelectromech. Syst. **14**(5), 987–999 (2005).
[23]C. Mishra and Y. Peles, "Cavitation in flow through a micro-orifice inside a silicon microchannel," Phys. Fluids **17**(1), 013601 (2005).
[24]K. S. Im, S. K. Cheong, C. F. Powell, M. C. D. Lai, and J. Wang, "Unraveling the geometry dependence of in-nozzle cavitation in high-pressure injectors," Sci. Rep. **3**(1), 1–5 (2013).
[25]Z. J. Jin, Z. X. Gao, X. J. Li, and J. Y. Qian, "Cavitating flow through a micro-orifice," Micromachines **10**(3), 191 (2019).
[26]M. Dular, I. Khlifa, S. Fuzier, M. Adama Maiga, and O. Coutier-Delgosha, "Scale effect on unsteady cloud cavitation," Exp. Fluids **53**(5), 1233–1250 (2012).
[27]M. Ghorbani, "The hydrodynamic cavitation manifestation in small chips," IEEE Access **9**, 110517–110524 (2021).
[28]M. Ghorbani, A. K. Sadaghiani, L. G. Villanueva, and A. Koşar, "Hydrodynamic cavitation in microfluidic devices with roughened surfaces," J. Micromech. Microeng. **28**(7), 075016 (2018).
[29]A. S. Aghdam, M. Ghorbani, G. Deprem, F. Ç. Cebeci, and A. Koşar, "A new method for intense cavitation bubble generation on layer-by-layer assembled SLIPS," Sci. Rep. **9**(1), 1–13 (2019).
[30]A. Hosseinpour Shafaghi, F. Rokhsar Talabazar, M. Zuvin, M. Talebian Gevari, L. G. Villanueva, M. Ghorbani, and A. Koşar, "On cavitation inception and cavitating flow patterns in a multi-orifice microfluidic device with a functional surface," Phys. Fluids **33**(3), 032005 (2021).
[31]G. Zhang, I. Khlifa, K. Fezzaa, M. Ge, and O. Coutier-Delgosha, "Experimental investigation of internal two-phase flow structures and dynamics of quasi-stable sheet cavitation by fast synchrotron x-ray imaging," Phys. Fluids **32**(11), 113310 (2020).
[32]S. Barre, J. Rolland, G. Boitel, E. Goncalves, and R. F. Patella, "Experiments and modeling of cavitating flows in venturi: Attached sheet cavitation," Eur. J. Mech. B Fluids **28**(3), 444–464 (2009).
[33]E. J. Foeth, C. W. H. Van Doorne, T. Van Terwisga, and B. Wieneke, "Time resolved PIV and flow visualization of 3D sheet cavitation," Exp. Fluids **40**(4), 503–513 (2006).
[34]A. Y. Kravtsova, D. M. Markovich, K. S. Pervunin, M. V. Timoshevskiy, and K. Hanjalić, "High-speed visualization and PIV measurements of cavitating flows around a semi-circular leading-edge flat plate and NACA0015 hydrofoil," Int. J. Multiphase Flow **60**, 119–134 (2014).
[35]F. Rokhsar Talabazar, M. Jafarpour, M. Zuvin, H. Chen, M. T. Gevari, L. G. Villanueva, D. Grishenkov, A. Koşar, and M. Ghorbani, "Design and fabrication of a vigorous 'cavitation-on-a-chip' device with a multiple microchannel configuration," Microsyst. Nanoeng. **7**(1), 1–13 (2021).
[36]A. Šarc, T. Stepišnik-Perdih, M. Petkovšek, and M. Dular, "The issue of cavitation number value in studies of water treatment by hydrodynamic cavitation," Ultrason. Sonochem. **34**, 51–59 (2017).
[37]S. S. Sawant, A. C. Anil, V. Krishnamurthy, C. Gaonkar, J. Kolwalkar, L. Khandeparker, D. Desai, A. V. Mahulkar, V. V. Ranade, and A. B. Pandit, "Effect of hydrodynamic cavitation on zooplankton: A tool for disinfection," Biochem. Eng. J. **42**(3), 320–328 (2008).

[38]P. Pipp, M. Hočevar, and M. Dular, "Challenges of numerical simulations of cavitation reactors for water treatment – An example of flow simulation inside a cavitating microchannel," Ultrason. Sonochem. **77**, 105663 (2021).
[39]E. Hutli, M. S. Nedeljkovic, N. A. Radovic, and A. Bonyár, "The relation between the high speed submerged cavitating jet behaviour and the cavitation erosion process," Int. J. Multiphase Flow **83**, 27–38 (2016).
[40]M. Omelyanyuk, A. Ukolov, I. Pakhlyan, N. Bukharin, and M. El Hassan, "Experimental and numerical study of cavitation number limitations for hydrodynamic cavitation inception prediction," Fluids **7**(6), 198 (2022).
[41]M. Ge, G. Zhang, M. Petkovšek, K. Long, and O. Coutier-Delgosha, "Intensity and regimes changing of hydrodynamic cavitation considering temperature effects," J. Clean Prod. **338**, 130470 (2022).
[42]D. Bauer, H. Chaves, and C. Arcoumanis, "Measurements of void fraction distribution in cavitating pipe flow using x-ray CT," Meas. Sci. Technol. **23**(5), 055302 (2012).
[43]A. Cioncolini, F. Scenini, and J. Duff, "Micro-orifice single-phase liquid flow: Pressure drop measurements and prediction," Exp. Therm. Fluid Sci. **65**, 33–40 (2015).
[44]A. Simpson and V. V. Ranade, "Modelling of hydrodynamic cavitation with orifice: Influence of different orifice designs," Chem. Eng. Res. Des. **136**, 698–711 (2018).
[45]M. Khavari, A. Priyadarshi, J. Morton, K. Porfyrakis, K. Pericleous, D. Eskin, and I. Tzanakis, "Cavitation-induced shock wave behaviour in different liquids," Ultrason. Sonochem. **94**, 106328 (2023).
[46]J. Morton, M. Khavari, A. Priyadarshi, A. Kaur, N. Grobert, J. Mi, K. Porfyrakis, P. Prentice, D. G. Eskin, and I. Tzanakis, "Dual frequency ultrasonic cavitation in various liquids: High-speed imaging and acoustic pressure measurements," Phys. Fluids **35**(1), 017135 (2023).
[47]M. Khavari, A. Priyadarshi, A. Hurrell, K. Pericleous, D. Eskin, and I. Tzanakis, "Characterization of shock waves in power ultrasound," J. Fluid Mech. **915**, R3 (2021).
[48]B. Puneeth, M. B. Kulkarni, S. Goel, P. Gravesen, J. Branebjerg, and O. S. Jensen, "Microfluidics-a review," J. Micromech. Microeng. **3**(4), 168 (1993).